A&A 490, 77–86 (2008)
DOI: 10.1051/0004-6361:200809909

Astronomy & Astrophysics

LABOCA observations of nearby, active galaxies

A. Weiß, A. Kovács, R. Güsten, K. M. Menten, F. Schuller, G. Siringo, and E. Kreysa

Max-Planck-Institut für Radioastronomie, Auf dem Hügel 69, 53121 Bonn, Germany
e-mail: aweiss@mpifr-bonn.mpg.de

Received 4 April 2008 / Accepted 17 August 2008

ABSTRACT

We present large scale 870 μm maps of the nearby starburst galaxies NGC 253 and NGC 4945 as well as the nearest giant elliptical radio galaxy Centaurus A (NGC 5128) obtained with the newly commissioned Large Apex Bolometer Camera (LABOCA) operated at the Atacama Pathfinder Experiment telescope. Our continuum images reveal for the first time the distribution of cold dust at a angular resolution of 20″ across the entire optical disks of NGC 253 and NGC 4945 out to a radial distance of 10′ (7.5 kpc). In NGC 5128 our LABOCA image also shows, for the first time at submillimeter wavelengths, the synchrotron emission associated with the radio jet and the inner radio lobes. From an analysis of the 870 μm emission in conjunction with ISO-LWS, IRAS and long wavelengths radio data we find temperatures for the cold dust in the disks of all three galaxies of 17−20 K, comparable to the dust temperatures in the disk of the Milky Way. The total gas mass in the three galaxies is determined to be 2.1, 4.2 and 2.8 $\times$ 10^9 $M_\odot$ for NGC 253, NGC 4945 and NGC 5128, respectively. The mass of the warmer (30−40 K) gas associated with the central starburst regions in NGC 253 and NGC 4945 only accounts for ∼10% of the total gas mass. A detailed comparison between the gas masses derived from the dust continuum and the integrated CO(1−0) intensity in NGC 253 suggests that changes of the CO luminosity to molecular mass conversion factor are mainly driven by a metallicity gradient and only to a lesser degree by variations of the CO excitation. An analysis of the synchrotron spectrum in the northern radio lobe of NGC 5128 shows that the synchrotron emission from radio to the ultraviolet (UV) wavelengths is well described by a broken power law and that the break frequency is a function of the distance from the radio core as expected for aging electrons. We derive an outflow speed of ∼0.5 c at a distance of 2.6 kpc from the center, consistent with the speed derived in the vicinity of the nucleus.

Key words. galaxies: starburst – galaxies: ISM – galaxies: jets – ISM: dust, extinction – radio continuum: ISM – infrared: ISM

1. Introduction

Nearly half the bolometric luminosity in the local universe is emitted at mid- and far-infrared (IR) wavelengths. The IR radiation is produced by warm interstellar dust grains that are heated by UV photons from hot high mass stars. This thermal emission of dust grains therefore carries valuable information on feedback processes from star formation, the chemical composition of the interstellar medium (ISM) and also on the total amount of interstellar matter in galaxies, the gas surface density and its relation to star-forming regions. The high spatial resolution of the Spitzer Space Telescope has greatly improved our view in this important wavelength range and allows for the first time to study spatially resolved spectral energy distributions (SEDs) across galaxies and the relation of IR emission to other tracers of star formation.

In order to provide a complete measurement of the dust SED it is highly desirable to combine the IR observations with data on the long wavelength (Rayleigh-Jeans) tail of the SED in the submm regime (see, e.g., Draine et al. 2007). This is because the submm observations are particularly sensitive to cold dust which dominates the dust mass in galaxies.

Ground based observations of the submm emission of nearby galaxies, however, remain a challenging task because they largely suffer from limitations due to the Earth's atmosphere. Furthermore, existing submm cameras have been limited in their field of view (FoV) to a few arc minutes which makes it difficult to survey large areas on the sky in a reasonable amount of time.

With the commissioning of the Large APEX Bolometer Camera (LABOCA, Siringo et al. 2007, and in prep.) at the APEX telescope (Güsten et al. 2006) at 5100 m altitude on Chajnantor this situation has largely improved. With its large field of view and large number of detectors in combination with the extremely dry conditions at the site, LABOCA provides the mapping-speed and sensitivity required to survey large areas on the sky down to mJy noise levels.

In this paper we present the first large scale 870 μm maps by LABOCA towards two nearby starburst galaxies NGC 253 and NGC 4945, and towards the nearest giant elliptical radio galaxy Cen A (NGC 5128). In Sect. 2 we describe the LABOCA observations and the data reduction, Sect. 3 focuses on the dust SEDs and gas masses. In Sect. 4 we discuss the thermal and non-thermal emission processes in our target galaxies and Sect. 5 summarizes our results.

2. Observations and data reduction

Observations were carried out using LABOCA on APEX. LABOCA is an array of 295 composite bolometers with neutron-transmutation-doped (NTD) germanium thermistors. The bolometers are AC-biased and operated in total power mode. Real-time signal processing of the 1 KHz data stream includes digital anti-alias filtering and down-sampling to 25 Hz. The radiation is coupled onto the detectors through an array of conical feed horns whose layout leads to a double beam spaced distribution of the individual beams in a hexagonal configuration over the 11.′4 field of view. The center frequency of LABOCA is 345 GHz and its passband has a *FWHM* of ∼60 GHz. The measured angular resolution of each beam is 19.″2.

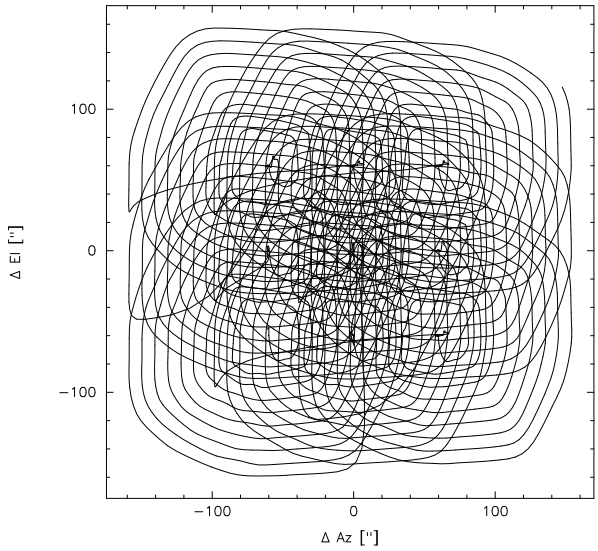

Fig. 1. Azimuth-Elevation path of the central bolometer of the array for a single raster of spiral scan as used for the observations.

The observations were carried out in 2007 July and August in mostly excellent weather conditions (precipitable water vapor (PWV) typically 0.5 mm, corresponding to a zenith opacity of 0.2 at the observing wavelength). Mapping was performed using a raster of spirals pattern. In each scan, the telescope traces a set of spirals with radii between 20″ and 1.6′ at nine raster positions separated by 60″ in azimuth and elevation (see Fig. 1). The pattern leads to a fully sampled map of the LABOCA FoV in a single scan. The radii and spacings of the spirals were optimized for uniform noise coverage across the FoV, while keeping telescope overheads at a minimum. The scanning speed varies between 0.5′–2.5′ s^{-1}, modulating the source signals even from a wide range of scales into the useful post-detection frequency band (0.1 to 12.5 Hz) of LABOCA, while providing at least 3 measurements per beam at the data rate of 25 samples per second even at the highest scanning velocity.

Calibration was achieved through observations of Mars, Uranus and Neptune as well as secondary calibrators and was found to be accurate within 9% rms. The atmospheric attenuation was determined via skydips every ∼2 h as well as from independent data from the APEX radiometer which measures the line of sight water vapor column every minute. The zenith opacities determined from both methods correlate well in general but the radiometer opacities are on average 30% higher than the values derived from the skydips. Details on the opacity determination and its limitations will be given by Siringo et al. (in prep.). We used a linear combination of both values for the data described here, with weights chosen such that they provide the most consistent calibrator fluxes for a wide range of opacities and source elevations.

Focus settings were determined typically once per night and checked during sunrise. Pointing was checked on nearby quasars and found to be stable within 3″ rms.

As all of our target galaxies are larger than the FoV of LABOCA, maps centered at several pointings were made towards each galaxy. The final maps consist of 3 pointings for NGC 253 and NGC 4945 and 5 pointings for Cen A. The total on source observing time is 8 h, 3 h and 5 h for NGC 253, NGC 4945 and Cen A respectively.

The data was reduced using the BoA reduction package (Schuller et al., in prep.). Reduction steps on the time series (time ordered data of each bolometer) include temperature drift correction based on two "blind" bolometers (whose horns have been sealed to block the sky signal), flat fielding, calibration, opacity correction, correlated noise removal on the full array as well as on groups of bolometers related by the wiring and in the electronics, flagging of unsuitable data (bad bolometers and/or data taken outside reasonable telescope scanning velocity and acceleration limits) as well as de-spiking. Each reduced scan was then gridded into a spatial intensity and weighting map. Weights are calculated based on the rms of each time series contributing to a certain grid point in the map. Individual maps were co-added noise-weighted and finally smoothed to an angular resolution of 20″. The resulting rms noise level for the central part of the maps is 3.5, 5.5 and 4.0 mJy/beam for NGC 253, NGC 4945 and Cen A, respectively. The final maps are shown in Figs. 2, 4 and 6.

The correlated noise removal implies that structures of a size similar to the angular separation on the sky between bolometer involved in the de-correlation will be removed from our maps (for details see e.g. Kovács et al. 2008). This effect is most pronounced for the correlated noise removal based on the wiring which typically involves 20 bolometers covering angular scales of 5′ × 1.5′ on sky. As a result, some of the faint, extended emission may have been filtered in our reduction. However, owing to the substantial field rotation (vs. the array alignment) over the span of the observations, we expect to fully recover scales up to 5′ along all spatial directions in our reductions. Since all of our targets are close to edge-on systems, with minor axes below this limiting scale, most of the large scale emission should be adequately recovered in the analysis.

3. Results

3.1. NGC 253

870 μm morphology: the 870 μm distribution in the central region of NGC 253 is dominated by the compact, well studied nuclear starburst region (see Fig. 2). Fitting a two-dimensional Gaussian intensity distribution yields a deconvolved size (*FWHM*) of 30″ × 16″ (370 × 200 pc at an assumed distance of 2.5 Mpc, Houghton et al. 1997) and a total flux is 6.4 ± 0.7 Jy. The dust surrounding the central starburst region closely follows the stellar bar visible at near infrared wavelengths (for an overlay of the 870 μm emission onto a NIR *K* band image see Fig. 2 right). The dust distribution in this inner part of NGC 253 is consistent with previously published Submillimeter Common User Bolometer Array (SCUBA) maps (Alton et al. 1999). The large scale dust distribution is dominated by two prominent spiral arms which originate near the stellar bar and are detected throughout the optical disk of NGC 253 out to a distance of 10′ from the nucleus. More diffuse emission is detected towards the trailing edge of the disk. Our LABOCA map does not show significant dust continuum emission associated with the outflow along the minor axis of NGC 253 (e.g. McCarthy et al. 1987; Fabbiano 1988; Dahlem et al. 1998). The total 870 μm flux detected towards NGC 253 is 17.6 ± 1.8 Jy.

Dust temperature and mass: the dust temperature distribution in NGC 253 has been investigated by Radovich et al. (2001) and Melo et al. (2002) based on ISOPHOT and IRAS mid and far-IR observations. Their analysis, however, does not include data on the Rayleigh-Jeans tail of the dust spectrum (except for the nuclear region of NGC 253) which could potentially hamper the identification of cold dust.

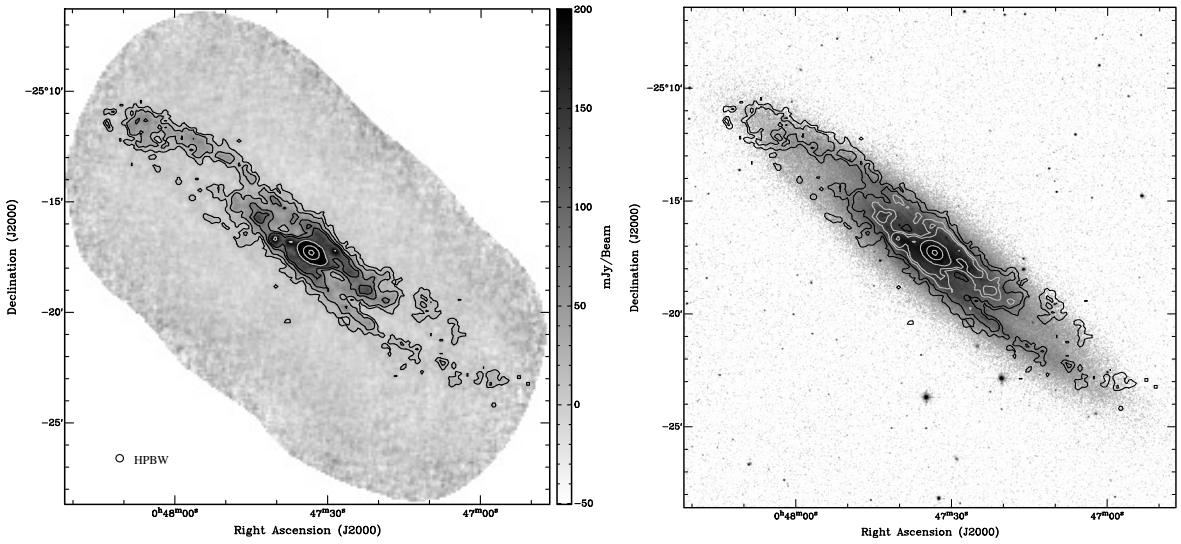

Fig. 2. *Left*: LABOCA 870 μm flux density map of NGC 253 smoothed to a spatial resolution of 20″. Contours are shown for 0.01, 0.03, 0.07, 0.1 (black) and 0.2, 1.0, 3.0 Jy/beam (grey). *Right*: 870 μm contours overlaid onto a 2MASS K-band image of NGC 253. Contour levels are the same as in *the left part* of the figure but only the two lowest levels are shown in black.

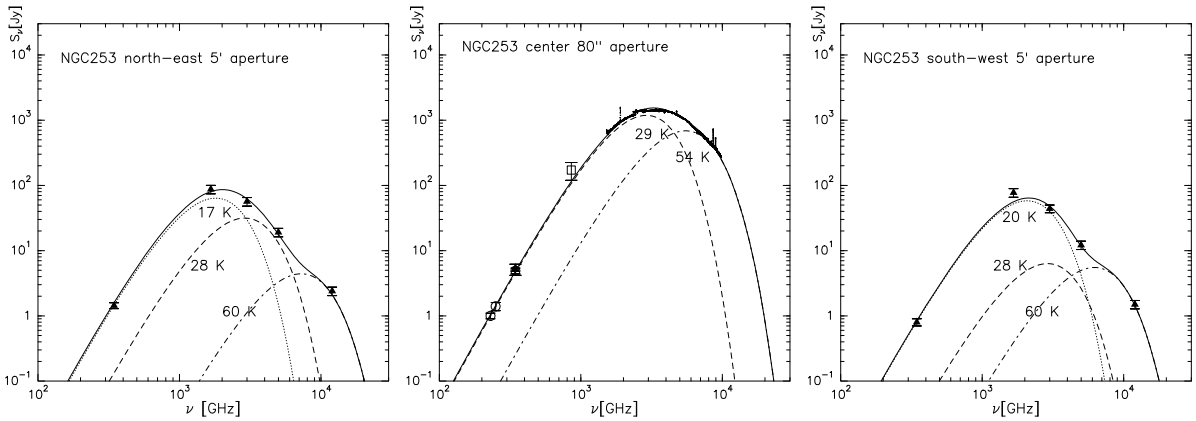

Fig. 3. Spectral energy distributions towards the north-east (*left*), center (*middle*) and south-west (*right*) of NGC 253. The 180, 100, 60 and 25 μm data points in the NE and SW are from Radovich et al. (2001). The 1.3 mm and 350 μm data in the center are from Krügel et al. (1990) and Rieke et al. (1973).

We have reanalyzed the dust temperatures in NGC 253 in the circular apertures c and d defined by Radovich et al. including our 870 μm fluxes. These apertures have diameters of 5′ centered well outside the nucleus on the north-eastern (c) and south-western (d) part of the disk (see Fig. 3 in Radovich et al. 2001). The 870 μm fluxes derived from our LABOCA map are 1.4 ± 1.5 and 0.8 ± 0.15 Jy for aperture c and d respectively. Note that the additional apertures e and f in Radovich et al., centered at the northern and southern outflow, are outside the field covered by our LABOCA observations.

As the optically thin approximation does not necessarily hold in the far/mid-IR regime, the dust emission was modeled using

$$S_\nu = \Big(B_\nu(T_{\rm dust}) - B_\nu(T_{\rm BG})\Big)\Big(1 - {\rm e}^{-\tau_\nu}\Big)\,\Omega_{\rm s}, \quad (1)$$

where B_ν is the Planck function, τ_ν the opacity and $\Omega_{\rm s}$ the source solid angle. The dust optical depth was computed using:

$$\tau_\nu = \kappa_{\rm d}(\nu)\, M_{\rm dust}/(D^2\,\Omega_{\rm s}), \quad (2)$$

where $\kappa_{\rm d}$ is the dust absorption coefficient, $M_{\rm dust}$ the dust mass and D is the distance to the source. For the frequency dependence of the dust absorption coefficient we adopt

$$\kappa_{\rm d}(\nu) \;=\; 0.04\,(\nu/250\;{\rm GHz})^{\beta} \quad (3)$$

with units of m^2 per kilogram of dust (Krügel & Siebenmorgen 1994), and with $\beta = 2$ (Priddey & McMahon 2001).

The observed dust SEDs for the two apertures are shown in Fig. 3 (left and right). Both SEDs require a fit with at least 3 temperature components to account for all observed fluxes between 870 μm and 25 μm. The dust SED for the north-eastern aperture is well described by a 17 K and a 28 K dust component for observations up to 60 μm. The 25 μm observations require higher dust temperatures and we have added, for illustration purposes, a 60 K component to both SEDs. For the south-western aperture the 180 μm flux is too high in comparison to our LABOCA flux so that both data points cannot be fit with a single dust temperature. The IRAS 100 μm point, however, limits the temperature of the cold dust to ≤20 K and we in the following therefore adopt a dust temperature of 17 K for the entire disk of NGC 253.

We note that the disk SED for NGC 253 (as well as for NGC 4945 and Cen A) is also consistent with additional cold gas

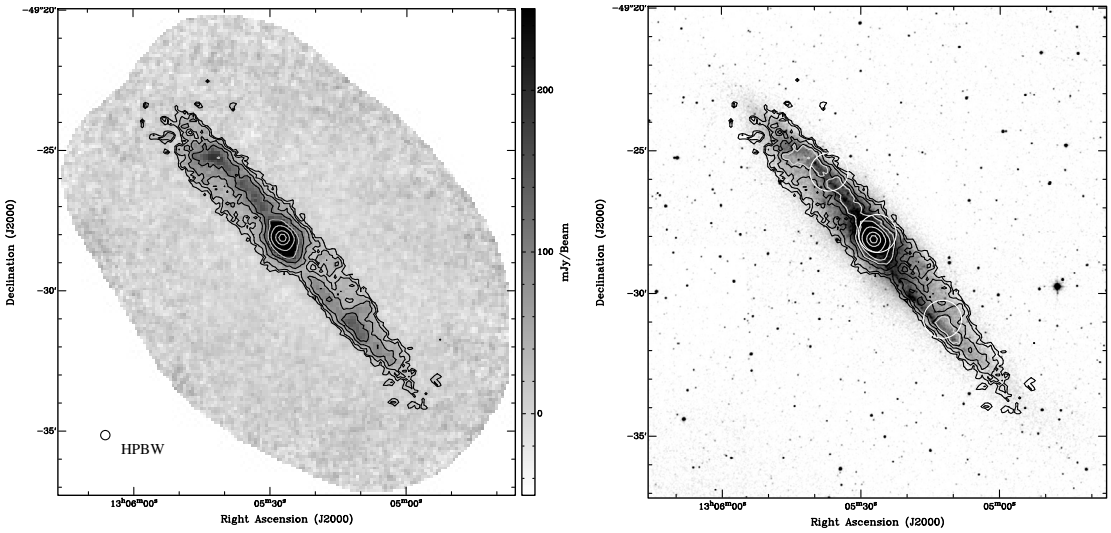

Fig. 4. *Left*: LABOCA 870 μm flux density map of NGC 4945 smoothed to a spatial resolution of 20″. Contours are show at 0.015, 0.03, 0.06, 0.1 (black) and 0.2, 0.5, 2.0, 4.0 Jy/beam (grey). *Right*: 870 μm contours overlaid onto a 2MASS *K*-band image of NGC 4945. Contour levels for 870 μm are the same as in *the left part* of the figure with an additional grey contour at 0.11 Jy/beam. The circles show the apertures of the ISO LWS observations.

below 10 K if the mass for the 17 K dust component is reduced. From our SED fits we find that such cold gas could contribute about 30−40% to the observed 870μm flux.

We have also reanalyzed the dust SED towards the center of NGC 253. At FIR wavelengths we used archival ISO Long-Wavelength Spectrometer (LWS) and Short-Wavelength Spectrometer (SWS) observations which continously cover wavelengths between 30 and 197 μm. The LABOCA flux in the 80″ aperture of the ISO spectra is 7.5 ± 0.8 Jy. We used the CO(3−2) observations by Dumke et al. (2001) to correct for the CO line emission in our 60 GHz bandwidth. The CO(3−2) line contributes 1.7 Jy (~20%). In addition we have used the 1.3 mm (Sakamoto et al. 2006), 1.3 mm (Krügel et al. 1990), corrected for 25% contribution from CO(2−1), (Mauersberger et al. 1996) and 350 μm (Rieke et al. 1973) fluxes towards the center of NGC 253.

The SED towards the center is well described by a two component dust model. The dust temperatures, however, depend on the underlying source solid angle. If e.g. we assume that the true source size matches the deconvolved source size derived above (30″ × 17″) we get dust temperatures of 30 and 55 K. Even for this large source size the dust optical depth is not negligible in the FIR regime ($\tau_{100\,\mu\mathrm{m}} = 0.31$). If we assume that the deconvolved source size has an area filling factor of only 10%, as suggested from CO line observations at similar spatial resolution (Mauersberger et al. 1996), the FIR opacities increase to $\tau_{100\,\mu\mathrm{m}} = 3$ and the dust temperature for the colder component increases to 37 K. In any case the mm/submm fluxes in the central 80″ region of NGC 253 are dominated by the warm central starburst region and do not show strong evidence for dust with temperatures below 30 K.

We use our coldest dust temperature estimate in the disk and in the nucleus to calculate the total gas mass of NGC 253 from the optically thin 870 μm emission:

$$M_{\mathrm{gas}} = S_{870}\, D^2\, \kappa^{-1}_{\mathrm{gas}\,870} \left(B_{870,T_{\mathrm{dust}}} - B_{870,T_{\mathrm{BG}}} \right)^{-1}. \quad (4)$$

Using $\kappa_{\mathrm{gas}\,870} = 0.0005\ \mathrm{m^2\ kg^{-1}}$, which corresponds to a 870 μm emissivity according to Eq. (3) and a gas to dust mass ratio of 150, we derive a total gas mass of $M_{\mathrm{total}} \approx 2.1 \times 10^9\ M_\odot$. The gas mass associated with the warm (35 K) dust in the nuclear region is $M_{\mathrm{center}} \approx 3.0 \times 10^8\ M_\odot$.

3.2. NGC 4945

870 μm morphology: the LABOCA 870 μm map of NGC 4945 is shown in Fig. 4 (left). The bright central starburst region has a deconvolved size of 19″ × 15″ (*FWHM*, 370 × 280 pc at a distance of 3.8 Mpc, Karachentsev et al. 2007) and an integrated flux of 7.2 ± 0.8 Jy. The dust emission from the disk of NGC 4945 follows closely the spiral arms visible in the *K*-band (see Fig. 4, right). Weak 870 μm emission is detected across the entire optical disk. The diffuse emission on the north-eastern trailing side of the galaxy is visible as strong dust absorption in optical *B*-band images. The total 870 μm flux detected in NGC 4945 is 15.8 ± 1.6 Jy.

Dust temperature and mass: for the determination of dust temperatures in the center of NGC 4945 we have used archival ISO LWS data ranging from 43 to 197 μm. ISO also observed two additional positions in the NE and SW part of the disk. The ISO pointings are shown as circles in Fig. 4 (right). These two observations only cover wavelengths shorter than 183 μm and show high noise below 50 μm. The noisy part has been omitted in the analysis. The dust SEDs of the three regions are shown in Fig. 5. As NGC 4945 contains an AGN (e.g. Madejski et al. 2000) we have estimated the contribution of non-thermal emission to the observed 870 μm flux density in the center using radio observations between 0.4 and 8 GHz. We find that the non-thermal contribution is negligible at 870 μm (~0.13 Jy, see Fig. 5 center). The dust SEDs at all three positions are well described by a two component dust model. The dust SEDs in the NE and SW are very similar and both are fit by temperatures of 17 K and 28 K – similar to those derived above for the disk of NGC 253. The 28 K component in the disk of NGC 4945 is more pronounced than in NGC 253 and dominates the peak of the SEDs. The mass, however, is dominated by the 17 K component.

For the determination of the dust temperature in the central 80″ region we have used the high-spatial resolution 1.3 mm observations from the Submillimeter Array (SMA, Chou et al. 2007) to disentangle emission from the warm, compact

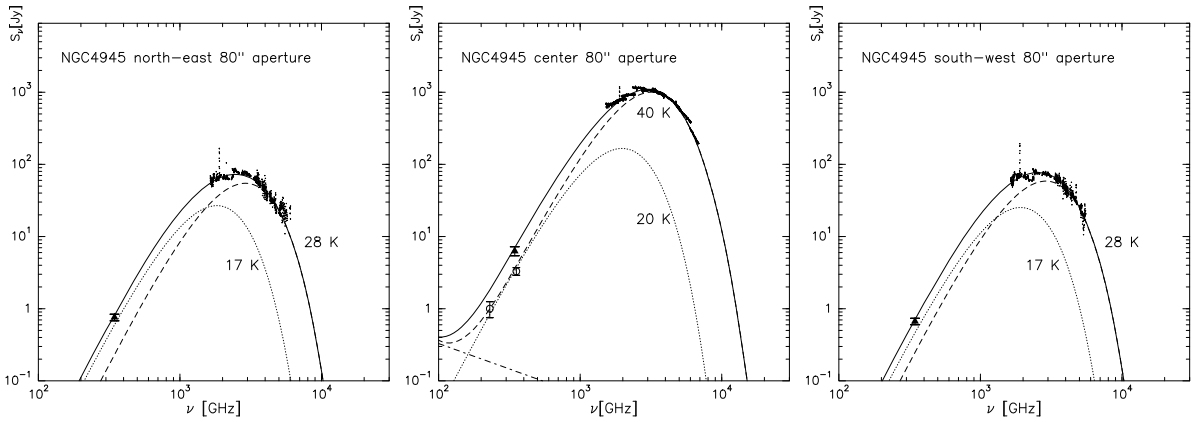

Fig. 5. Spectral energy distributions towards the north-east (*left*), center (*middle*) and south-west (*right*) of NGC 4945 measured in a 80″ aperture. The location of the apertures is shown in Fig. 4 (*right*). The mid-IR data are from archival ISO LWS observations. The open circles in the central plot represent the 1.2 mm and 870 μm fluxes associated with the 40 K gas in the central 185 × 95 pc (Chou et al. 2007). The dashed dotted line for the center of NGC 4945 shows the non-thermal contribution of the AGN to the spectrum.

starburst region and the disk. As the 1.3 mm continuum emission is more compact than the LABOCA beam (10″ × 5″) we first fit a warm dust component to the integrated SMA flux, the flux in the central LABOCA beam (3.3 Jy, CO line corrected) and the FIR ISO spectrum using Ω_s = 56 arcsec^2, the source solid angle from the 1.3 mm SMA continuum observations. This approach is justified as most of the FIR emission also arises from a region smaller than the LABOCA resolution (Brock et al. 1988). The contribution from the CO(3−2) line to the LABOCA flux was estimated using the flux densities from Wang et al. (2004) and found to be of order 20%. This yields a dust temperature of 40 K for the central 10″ × 5″. The observed 870 μm flux (also corrected for 20% line contribution) and the long ISO wavelengths for the full 80″ aperture requires an additional cold dust component which is well described with a temperature of 20 K. Similar to our results on NGC 253, the FIR opacity in the nuclear region is high with $\tau_{100\,\mu m}$ = 1.1, in agreement with the lower limit from Brock et al. (1988).

With the temperatures of the coldest, mass dominating dust components in the disk (17 K) and in the center (20 K) we obtain a total gas mass for NGC 4945 of $M_{\rm total} \approx 4.2 \times 10^9\ M_\odot$ of which $1.2 \times 10^9\ M_\odot$ are located in the central 1.4 kpc. The warm (40 K) gas mass associated with the IR luminous central 185 × 95 pc is $3.8 \times 10^8\ M_\odot$.

3.3. Cen A (NGC 5128)

Our LABOCA map of NGC 5128 shows four distinct emission features: 1) the bright, central radio core which is blended with the central dust disk, 2) the northern, and 3) southern radio lobes, and 4) some faint emission associated with the optical dust absorption lanes in the outer parts of the galaxy. Emission from the lobes is detected for the first time at submm wavelengths and its distribution follows closely that of the radio emission at cm wavelengths (Condon et al. 1996, see Fig. 6). They are discussed in more detail in Sect. 4.4. The central dust disk has a pronounced S-shape and is very similar in structure to what has been observed in previous SCUBA and ISOCAM images at 850 and 450 μm as well as at 15 and 7 μm (Mirabel et al. 1999; Leeuw et al. 2002).

The total flux in our map is 18.0 ± 1.7 Jy out of which 3.3 ± 0.4 Jy are associated with the radio lobes. The unresolved central core has a flux density of 6.4 ± 0.7 Jy which is lower than the 850 μm flux of 8.1 ± 0.8 Jy reported by Leeuw et al. (2002). This may suggest long term variability of the AGN in NGC 5128 up to submm wavelengths. Nevertheless calibration uncertainties or the effective reconstruction of the underlying extended dust disk may play a role too.

The dust temperatures in the disk were determined at three positions using our 870 μm fluxes in conjunction with archival ISO-LWS spectra observed towards the nucleus and at equatorial offsets of −53″, 27″ (NW) and 110″, −49″ (SE) from the center (Unger et al. 2000, Fig. 6, right). The south-eastern spectrum is very noisy for wavelengths below 55 μm and we have omitted these data from our analysis. The LABOCA fluxes in the 80″ ISO apertures are 0.5, 10.3 and 1.6 Jy for the SE, center and NW respectively. For the central aperture we have subtracted the 870 μm flux of the central radio core (6.4 Jy, see above) to correct for the non-thermal contribution in this region. This, however, only yields a proxy to the 870 μm dust emission as we expect also a non-thermal contribution from the jets emerging from the central engine. This is evident from the shallow spectral index between 850 and 450 μm in this region (Leeuw et al. 2002). The dust SEDs in the three regions are shown in Fig. 7.

All SEDs are well described by a two component dust model. For the warmer gas component we find in all three apertures a dust temperature of ∼30 K in agreement with the results from Unger et al. (2000). The cold component in the NE has a dust temperature of 19 K similar to the disk temperatures of NGC 253 and NGC 4945. In the SE our fit indicates that the cold gas may be slightly warmer with 22 K. The FIR spectrum in the SE, however, is quite noisy and the data is also consistent with 20 K. The SED fit to the central region yields a dust temperature of only 14 K – significantly lower than what was derived in the NW and SE. We note that this even holds if we have underestimated the non-thermal 870 μm contribution: in order to be consistent with a 19 K dust spectrum the 870 μm emission in the central aperture (after correcting for the flux from the radio core) needs to be dominated by the non-thermal emission from the jet which is inconsistent with the measured surface brightness from the southern radio lobe near the disk. The low temperature for the cold dust in the central region is consistent with the results from Leeuw et al. (2002) who derive 12 K albeit in a larger aperture. Our analysis, however, does not confirm their decreasing dust

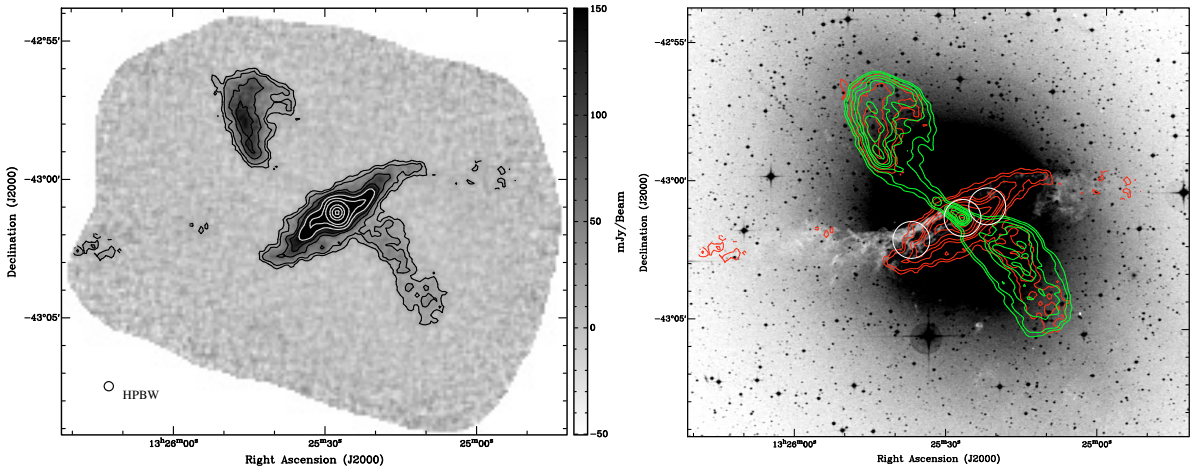

Fig. 6. *Left*: LABOCA 870 μm flux density map of Cen A (NGC 5128) smoothed to a spatial resolution of 20″. Contours are show at 0.015, 0.03, 0.07, 0.1 (black) and 0.15, 0.25, 0.5, 2.0, 4.0, 6.5 Jy/beam (grey). *Right*: 870 μm contours (red) overlaid onto a B-band image of Cen A from the SDSS archive. Contour levels for 870 μm are the same as in *the left part* of the figure. Green contours show the 1.4 GHz VLA radio continuum map (Burns et al. 1983). Contours correspond to 0.3, 0.5, 1.0, 1.5, 2.0, 3.0 and 4.5 Jy/beam. The circles correspond to the apertures observed by ISO.

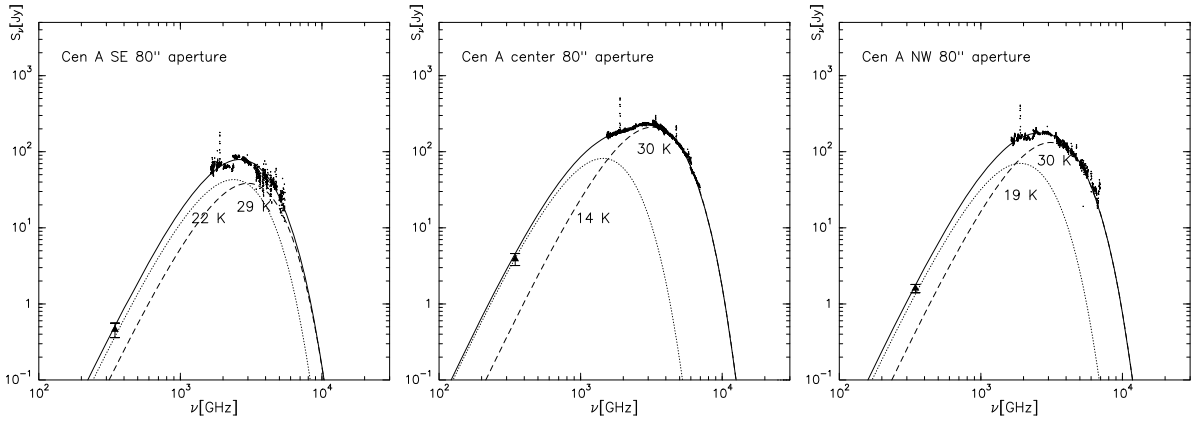

Fig. 7. Spectral energy distributions towards the south-east (*left*), center (*middle*) and north-west (*right*) of NGC 5128 measured in a 80″ aperture. The location of the apertures is shown in Fig. 6 (*right*). The FIR-IR data are from archival ISO LWS observations.

temperature of the warm component with increasing distance from the center.

Using 14 K for the the cold dust in the central aperture and 20 K as for the rest of the thermal 870 μm emission we derive a total gas mass for NGC 5128 of $M_{\rm total} \approx 2.8 \times 10^9\ M_\odot$ out of which $M_{\rm center} \approx 1.6 \times 10^9\ M_\odot$ are associated with the 14 K gas in the central 1.4 kpc (80″ aperture).

4. Discussion

4.1. Dust temperatures

Our dust temperature estimate for the coldest, mass carrying dust component of 17 K in the disk of NGC 253 is in excellent agreement with estimates based on lower resolution ISOPHOT and IRAS data (Melo et al. 2002; Radovich et al. 2001). The dust SEDs in the disks of NGC 4945 as well as NGC 5128 show similarly low dust temperatures, which suggests that the temperatures of the dust in the disks of all three active galaxies are comparable to those found in the Milky Way (MW, e.g. Cox & Mezger 1989). None of our target shows evidence for dust with temperatures below 10 K. This finding is also in agreement with results based on SCUBA and Spitzer observations of the SINGS galaxy sample (Draine et al. 2007). Our dust SEDs, however, do not rule out the presence of such cold gas. Its effect on the total dust/gas mass estimate, on the other hand, is not dramatic because a cold (e.g. a 8 K) dust component in the disks cannot contribute to more than ∼40% of the observed 870 μm flux in order to be consistent with the overall SED shape.

For the nuclear starburst regions our analysis suggests that NGC 253 is free of cold ($T < 30$ K) dust while the central SEDs for NGC 4945 and NGC 5128 both show a clear signature of dust at temperatures comparable to those found in the disks. This, however, does not necessarily imply that the nuclear starburst itself contains cold gas because the 80″ aperture analyzed here is still too large to separate spatially the central active region from the surrounding disk. For NGC 5128 the situation is further complicated by the strong non-thermal contribution from the central AGN and the jets to the 870 μm flux, which makes it difficult to determine the submm flux related to thermal dust emission alone. Therefore, the suggested decrease of the cold dust component's temperature from the disk towards the center in NGC 5128 may simply reflect an imperfect separation between the thermal and non-thermal flux contributions.

Table 1. Observed and derived dust properties of our target galaxies.

Target	D [Mpc]	Total observed Flux [Jy]	$T_{\rm dust,disk}$ [K]	$M_{\rm dust,disk}$ [10^6 $M_\odot$]	$T_{\rm dust,center}$ [K]	$M_{\rm dust,center}$ [10^6 $M_\odot$]	$M^a_{\rm gas,total}$ [10^9 $M_\odot$]
NGC 253	2.5	17.6 ± 1.8	17/28	11.7	35/55	2.0	2.1
NGC 4945	3.8	15.8 ± 1.6	17/28	19.8	20/40	5.7	4.2
NGC 5128	3.5	18.0 ± 1.7[b]	20/30	8.0	14/30	10.8	2.8

[a] Assuming a gas-to-dust mass ratio of 150; [b] non thermal contribution: 6.4 Jy (nucleus), 3.3 Jy (radio lobes).

4.2. Gas masses

Due to the large areas our target galaxies project on the sky, only few mm/submm observations have been published so far which allow to determine the total molecular gas content across the entire optical disks. For NGC 253, Houghton et al. (1997) have presented CO(1−0) observations having a similar extent than our LABOCA maps. They find a total molecular gas mass of 2.4×10^9 $M_\odot$ using a CO conversion factor of 3×10^{20} cm^{-2} (K km s^{-1})$^{-1}$. This value includes the contribution of heavier elements. The H I mass of NGC 253 is 1.8×10^9 $M_\odot$ (Koribalski et al. 2004) which yields a total mass of 4.2×10^9 $M_\odot$, a factor of 2 higher than our estimate based on the dust continuum. This may argue for a smaller CO conversion factor or a higher gas-to-dust mass ratio. Several studies have suggested that the average gas-to-dust mass ratio of a galaxy is a function of its enrichment (e.g. Draine et al. 2007; Engelbracht et al. 2008). Indeed the characteristic oxygen abundance (a measure for the average metallicity of a galaxy) in NGC 253 is lower by ∼0.1 dex than the MW's metallicity (Pilyugin et al. 2004). But such a small difference in metallicity is not expected to cause the higher gas-to-dust mass ratio in NGC 253 illustrated in Fig. 8 where we show the location of our target galaxies on the dust-to-gas mass ratio vs. characteristic oxygen abundance plot for the SINGS galaxies (Draine et al. 2007, their Fig. 16). NGC 253 lies well within the factor 2 scatter band on this metallicity relation observed for the SINGS galaxies. Given the simplifying assumptions made in our mass estimate (e.g. the constant dust absorption coefficient across the disk of NGC 253 and the use of constant CO conversion factor), the mass estimates for the dust continuum and the CO and H I are in reasonable agreement.

CO(1–0) observations covering the optical disk of NGC 4945 have been published by Dahlem et al. (1993). They give an H_2 mass of 2.2×10^9 $M_\odot$ (scaled to D = 3.8 Mpc and using a CO conversion factor of 2×10^{20} cm^{-2} (K km s^{-1})$^{-1}$). Correcting for heavier elements and taking the H I mass of 1×10^9 $M_\odot$ (Ott et al. 2001, scaled to D = 3.8 Mpc) into account yields a total gas mass of 4×10^9 $M_\odot$, in good agreement with our results. Our dust mass is also in agreement with the expected metallicity dependence for MW like dust (see Fig. 8). For the determination of the characteristic oxygen abundance we have used here the O/H−M_B relation for spiral galaxies from Pilyugin et al. (2004).

For NGC 5128 the situation is different as our estimated gas mass based on the dust emission exceeds those based on CO and H I by more than a factor of 4: Eckhart et al. (1990) derive a total molecular gas mass based on CO of 2.7×10^8 $M_\odot$ (scaled to D = 3.5 Mpc). The H I mass accounts for 2.5×10^8 $M_\odot$ (Gardner & Whiteoak 1976, scaled to D = 3.5 Mpc). Correcting for heavier elements this yields a total gas mass of 6×10^8 $M_\odot$ compared to our estimate of 2.8×10^9 $M_\odot$. We note that this discrepancy still holds if we would assume that the cold dust towards the center has a temperature of 20 K instead of the 14 K derived from our SED fitting (see discussion above).

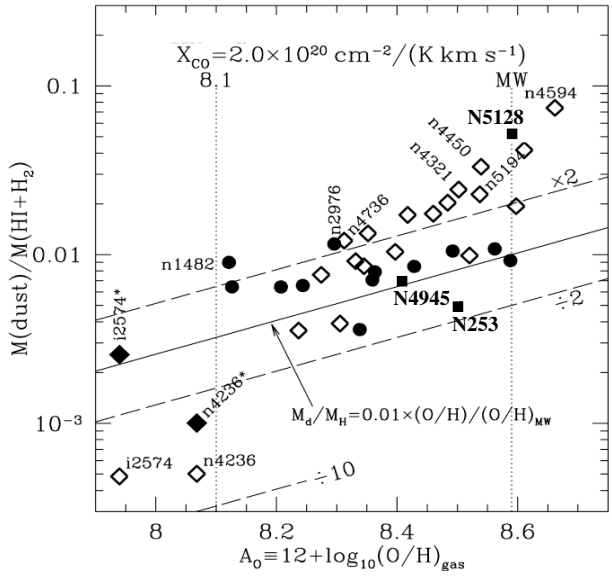

Fig. 8. Dust-to-gas mass ratio vs. characteristic oxygen abundance plot for the SINGS galaxies adopted from Draine et al. (2007, their Fig. 16). Our target galaxies are shown as filled squares. The CO intensities have been converted to H_2 masses using a conversion factor of 2.0×10^{20} cm^{-2} (K km s^{-1})$^{-1}$.

Based on SCUBA 850 and 450 μm observations, Leeuw et al. (2002) find a dust mass of 2.2×10^6 $M_\odot$ for the central 4.5 kpc which translates into a gas mass of 3.3×10^8 $M_\odot$ assuming a gas-to-dust mass ratio of 150 – a factor of two lower than the estimate based on CO and a factor of 8 lower than our estimate. This discrepancy is difficult to understand because our assumed dust absorption coefficient, κ_ν, differs at most by ∼30% from the values used by Leeuw et al. and our LABOCA flux is only slightly higher than the SCUBA 850 μm flux (7.8 Jy compared to 6.4 Jy adding the inner and outer disk as defined in Leeuw et al.). Furthermore, our dust temperature is somewhat higher than the 12 K derived by Leeuw et al., so that we would expect only a small difference between the two dust mass estimates. Using the dust temperatures, emissivities and 850 μm fluxes given in Leeuw et al. we indeed estimate dust and gas masses of 1.1×10^7 $M_\odot$ and 1.7×10^9 $M_\odot$ for NGC 5128 in better agreement with our results. Our higher dust masses are also in agreement with the results of Mirabel et al. (1999). Their 850 μm fluxes, however, are about a factor of 10 higher than those published by Leeuw et al. (2002) and from our LABOCA maps and their dust mass should therefore be treated with some caution. Independent estimates of the dust mass in NGC 5128 have been derived by Block & Sauvage (2000) using the V-15 μm ratio which results in $M_{\rm d}$ = 2.3×10^6 $M_\odot$ (scaled to D = 3.5 Mpc). This study, however, only addresses the dust content of the central 90″ and may miss diffuse dust which could significantly increase the estimated dust mass.

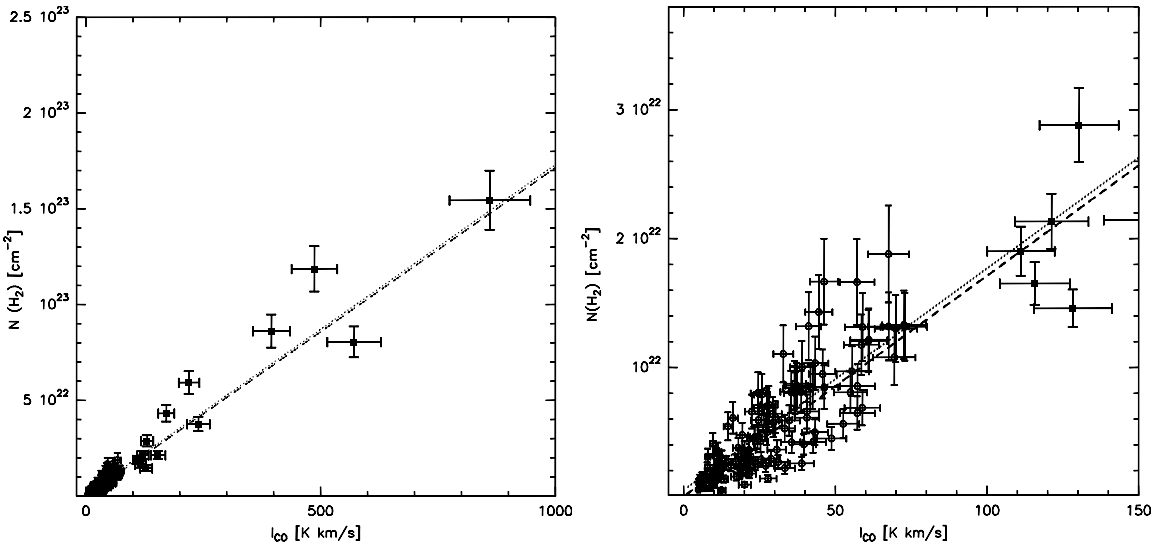

Fig. 9. Observed integrated CO(1–0) intensities (Sorai et al. 2000) compared to the H_2 gas column densities derived from our dust continuum analysis in NGC 253 corrected for the H I contribution. Filled squares show positions towards the central starburst region, open circles positions in the bar/disk of NGC 253. The dashed line is a linear fit to data in the starburst region only, the dotted line a fit to all other data points. *The right part* of the figure is a zoom to the full diagram shown on *the left*.

Considering these uncertainties in the dust mass in Cen A it is impossible to obtain strong conclusions by comparing the gas mass derived from CO and the dust continuum. We note, however, that the molecular gas mass derived by Eckart et al. (1990) is based on a standard galactic conversion factor and therefore unlikely to underestimate the gas mass by more than a factor of 2. Therefore, the high dust mass derived from our LABOCA data may suggest that the dust properties or the gas-to-dust mass ratio in NGC 5128 are different from those in NGC 253 and NGC 4945.

To our knowledge no oxygen abundance estimates across the disk of NGC 5128 has been published which would allow secure derivation of the characteristic oxygen abundance to check for metallicity effects as a possible reason for the low gas-to-dust mass ratio. Estimates based on the globular cluster systems of NGC5128 indicate metalicities similar to or somewhat higher than their MW counterparts (see Israel et al. 1998, and references therein). Using, as for NGC 4945, M_B as indicator for O/H leads to a similar result ($12+\log(\mathrm{O/H}) = -8.5$) although it is not clear if this relation holds for elliptical galaxies. We therefore assume a characteristic oxygen abundance similar to the MW which places NGC 5128 well above the expected metallicity dependence in Fig. 8.

4.3. CO intensity vs. dust column density in NGC 253

Among our target galaxies the CO emission in NGC 253 has been studied in most detail and large scale CO maps exist in the literature with similar spatial resolution than our LABOCA data. Sorai et al. (2000) imaged large parts of the optical disk in CO(1−0) at a spatial resolution of 16″ using the Nobeyama 45 m telescope. To investigate variations of the mass tracing capabilities of CO in comparison to the dust continuum we have compared their integrated CO intensities to the H_2 column densities derived from our LABOCA maps within the central 6 Kpc of NGC 253 taking the neutral gas mass fraction measured from H I into account. The gas mass (H I & H_2) distribution from the dust was computed using a dust temperature distribution as suggested from our dust SED analysis: 35 K within the central 30″ × 16″, 19 K out to a radial distance of 40″ (ISO aperture) and 17 K for emission further out and a constant gas-to-dust mass ratio of 150. This gas mass distribution was corrected for H I using the radial dependence of molecular gas mass fraction from Sorai et al. (2000, their Fig. 9a) and finally converted to a H_2 column density map.

The comparison between the H_2 column density and the integrated CO intensity was done for 20″ sized pixels after smoothing both data sets to that resolution and is shown in Fig. 9. From this figure there is no obvious difference between the CO conversion factor in the central starburst region and positions in the bar/disk region of NGC 253. A linear fit yields conversion factors of 1.7×10^{20} cm^{-2} (K km s^{-1})$^{-1}$ ($2.7\ M_\odot$ (K km s^{-1} pc^2)$^{-1}$) in both regions with errors of 3% and 7% for the central and the bar/disk region. The larger error for the slope outside the nuclear starburst region is mainly due to the smaller dynamic range of the data points. The result is little dependent on the neutral gas correction. For example, if we assume that all gas is in molecular form and ignore the H I (which maximizes the conversion factor), we find the same value for the nuclear region and an increase of only 50% (2.5×10^{20} cm^{-2} (K km s^{-1})$^{-1}$) for the bar/disk region.

This result is surprising at the first glance, as several detailed CO studies have suggested that the CO conversion factor is several times lower in the central starburst region (e.g. Mauersberger et al. 1996; Harrison et al. 1999, for the center of NGC 253) than the galactic conversion factor, which in turn is expected to be a good approximation for the regions outside the starburst. In contrast Fig. 9 hints at a constant conversion factor over the entire galaxy, including its nucleus. One must note, however, that in the strict sense, Fig. 9 implies a constant ratio only for the measured CO/dust masses (or fluxes) across the galaxy, while the conversion of these into total gas mass may both also depend on other characteristics. Specifically, our result is consistent with the possibility of both the gas/CO and the gas/dust ratios varying similarly with metalicities. For example, Mauersberger et al. (1996) assumed a metallicity of 3 times the solar value for their determination of the CO conversion factor in NGC 253. Matching this, a gas-to-dust mass ratio that scales

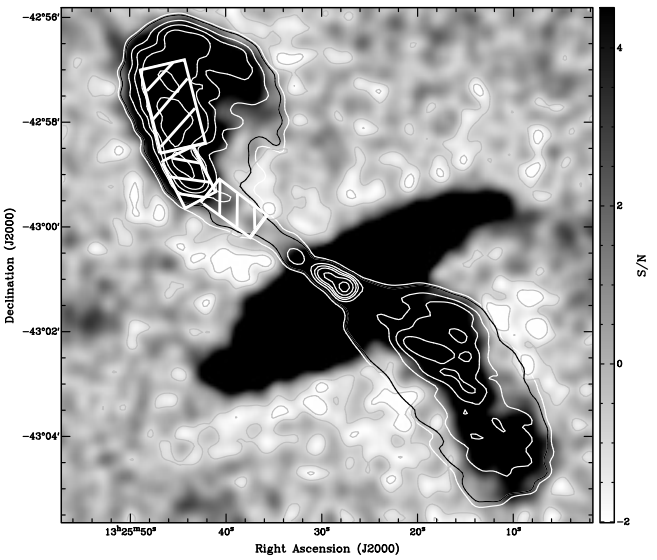

Fig. 10. High contrast representation of the signal to noise map of our 870 μm observations towards NGC 5128 smoothed to an effective spatial resolution of 25″ (beam smoothed). The negative parts of the image are highlighted by two grey contours with signal to noise ratios of −1 and −2. This presentation also shows the faint submm emission from the northern radio jet. The white and black contours are the 1.4 GHz VLA map from Condon et al. (1996). The white boxes indicate those regions which have been used to analyze the spectral index.

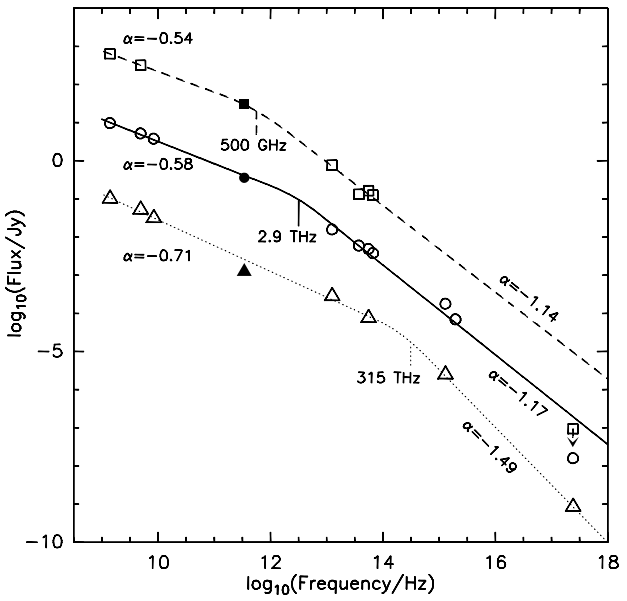

Fig. 11. Synchrotron spectra from radio to X-rays in three apertures in the northern radio lobe. The apertures are shown in Fig. 10 and correspond to the "outer" (shown as dashed line and square symbols), "middle" (solid, circles) and "inner" (dotted, triangles) region defined in Hardcastle et al. (2006). The filled symbols represent the 870 μm flux densities. For all other data see Table 1 in Hardcastle et al. (2006). The lines show broken power law fits to the data. The presentation for the outer/inner region have been up/down scaled by 1.5 dex.

inversely with metalicity, i.e. 50 (if a galactic value of 150 is assumed) for the nucleus of NGC 253, is implied by our results. The apparent constancy of the CO/dust ratio across NGC 253 also suggests that changes in the gas/CO conversion are unlikely to be dominated by the variation of CO excitation, since that would be apparent in deviations from the strict linear relation, which we do not see.

4.4. Radio lobes in Cen A

The 870 μm emission associated with the radio lobes is very similar in morphology to the 1.4 GHz continuum emission (Figs. 6 right and 10). As the synchrotron emission from the northern radio lobe has also been detected at 15−4.5 μm in the UV and at X-ray energies (Brookes et al. 2006; Hardcastle et al. 2006) it is clear that the 870 μm emission is synchrotron in nature and not associated with dust driven out from the disk by the radio jet. The southern radio lobe is detected for the first time at wavelengths shorter than 3.5 cm. We show a high contrast signal to noise map of our LABOCA observations in Fig. 10. From this image it is evident that the northern radio jet is also detected at 870 μm. The jet, however, is located in a low level negative bowl surrounding the strong central emission. Such negative artifacts are unavoidable byproducts of the skynoise removal which results in the filtering of low spatial frequencies. As a consequence the true 870 μm flux of the jet is difficult to determine. The 870 μm flux of the northern and southern lobes are 2.5 and 0.9 Jy respectively.

The variation of the spectral index of the northern lobe with wavelength has recently been investigated by Hardcastle et al. (2006) and Brookes et al. (2006). Based on Spitzer/IRAC, GALEX and Chandra data Hardcastle et al. fit the synchrotron emission by a broken power law. Their model with a break frequency at ∼300 GHz, however, underestimates the observed UV flux and also provides a poor fit to the observed slope between the IRAC bands. We have included our LABOCA fluxes in the analysis of the spectral index in the three regions in the northern lobe defined by Hardcastle et al. (see Fig. 10). These regions cover the radio jet (inner), the southern part of the radio lobe (middle) and the northern part of the lobe (outer region). The LABOCA flux within the three regions is 40 ± 20 mJy, 365 ± 40 mJy and 1.0 ± 0.1 Jy for the inner, middle and outer region respectively. The synchrotron spectra of the three regions are shown in Fig. 11. We fit the radio to X-ray data of all three regions with a non-standard ($\Delta\alpha \neq 0.5$), broken power law. For the inner region all data can well be fit with a break frequency of $\log_{10}(\nu_{\mathrm{b/Hz,inner}}) = 14.5 \pm 0.65$ (315 THz) and a change of the power index of $\Delta\alpha_{\mathrm{inner}} = 0.8 \pm 0.3$. Our LABOCA flux falls somewhat below the expected value from this model (68 mJy) which we attribute to the difficulties to determine the 870 μm flux density in this particular region as described above. Because the break frequency in the inner region falls into the NIR regime this data point, however, is not critical for the fitting. For the middle and the outer regions the break frequency shifts, as expected, to lower frequency yielding $\log_{10}(\nu_{\mathrm{b/Hz,middle}}) = 12.5 \pm 0.3$ (2.9 THz) and $\log_{10}(\nu_{\mathrm{b/Hz,outer}}) = 11.7 \pm 0.6$ (500 GHz). The change of the power index for both regions is close to that predicted by a continuous injection model (KP model) with $\Delta\alpha_{\mathrm{middle}} = 0.6 \pm 0.1$ and $\Delta\alpha_{\mathrm{outer}} = 0.6 \pm 0.15$. For both regions the broken power law model, however, overpredicts the X-ray flux, which indicates that the energy distribution of the electrons is more complex than a distribution yielding a simple broken power-law. A detailed modeling of the energy distribution is beyond the scope of this paper but we note, that also a single injection (SI) model with its exponential decrease at high energies does not provide a good fit to the data. From Fig. 11 it can be seen that a model intermediate between the SI and KP, e.g. a broken power law with a high energy exponential decrease, presumably gives a better description of the observed fluxes between the radio and X-ray.

For the inner jet region, where the broken power law fits all observed fluxes, we can also estimate the speed of the electrons using our fit to the break frequency: assuming a magnetic field strength of 3 nT, the minimum energy value (Brookes et al. 2006), we get an age of the electrons of ~17 000 yrs which yields a speed of 0.5 c using the measured projected distance of 2.6 kpc from the nucleus and a jet view angle of ~20° (Hardcastle et al. 2003). This speed is consistent with the electron speed derived close to the central source. (Hardcastle et al. 2003).

5. Summary

New large scale LABOCA 870 μm continuum images are presented for the starburst galaxies NGC 253, NGC 4945 and the nearest giant elliptical radio galaxy Cen A (NGC 5128). Our LABOCA images reveal for the first time the distribution of cold dust across the entire optical disks in NGC 253 and NGC 4945 out to a radial distance of 7.5 kpc. In NGC 5128 the 870 μm image shows not only the thermal emission from the central molecular gas disk and the optical absorption features but also the synchrotron emission from the central radio source, the northern radio jet and the inner radio lobes north and south of the disk. We have used the 870 μm emission in conjunction with ISO-LWS, IRAS and long wavelengths radio data to analyze the thermal dust emission in all three galaxies as well as the synchrotron emission in NGC 5128. Our main findings are summarized as follows:

Similar to the dust emission in the disk of the Milky Way the thermal dust emission at 870 μm in the disks of NGC 253, NGC 4945 and NGC 5128 is dominated on large scales by cold dust with temperatures of 17−20 K. We do not find evidence for significant flux from even colder gas at temperatures below 10 K.

In the active centers, the lowest dust temperature appears to be at 30−40 K. The dust SEDs of the central regions of NGC 4945 and NGC 5128 do, however, show the presence of gas at temperatures comparable to that of cold gas in the disks. From our analysis we cannot rule out that this gas is associated with the starburst region itself, but it appears more likely that this gas is also associated with the disks. Higher spatial resolution FIR data will be required so solve this issue.

Using a gas-to-dust mass ratio of 150 we derive total gas mass of 2.1, 4.2 and 2.8 $\times$ 10^9 $M_\odot$ for NGC 253, NGC 4945 and NGC 5128. While these estimates lead to consistent results compared to CO and H I measurements for NGC 253 and NGC 4945, our mass estimate for NGC 5128 exceeds published gas mass estimates by a factor of 4. This could suggest that the dust properties in NGC 5128 are different from those in other active galaxies. The strong contribution of non-thermal emission at 870 μm in NGC 5128, however, complicates the analysis.

A detailed comparison between the gas masses based on the dust continuum and the observed CO(1−0) intensity in NGC 253 shows no changes of the CO conversion factor towards the nuclear region if the gas-to-dust mass ratio is assumed to be constant across the galaxy. This suggests that at least for NGC 253 changes of the CO conversion factor are mainly driven by a metallicity gradient and only to a lesser degree by variations of the CO excitation.

The contribution of the non-thermal emission processes in NGC 5128 to the observed 870 μm flux accounts for almost 50%. The synchrotron spectrum (radio to the UV/X-rays) in the northern radio lobe is well described by a non-standard broken power-law spectrum. The break frequency is a function of the distance from the central radio source as expected for aging electrons. The break frequency of the synchrotron spectrum in the northern radio jet, 2.6 kpc from the center, suggests an outflow speed of 0.5 c, consistent with the speed derived very close to the nucleus.

Acknowledgements. We thank the APEX staff for their support during the LABOCA commissioning and observing run. We also thank K. Sorai for providing us with their Nobeyama 45 m CO(1−0) data as well as E. Krügel for many fruitful discussions.

References

Alton, P. B., Davies, J. I., & Bianchi, S. 1999, A&A, 343, 51
Block, D. L., & Sauvage, M. 2000, A&A, 353, 72
Brock, D., Joy, M., Lester, D. F., Harvey, P. M., & Ellis, H. B. Jr. 1988, ApJ, 329, 208
Brookes, M. H., Lawrence, C. R., Keene, J., et al. 2006, ApJ, 646, 41
Burns, J. O., Feigelson, E. D., & Schreier, E. J. 1983, ApJ, 273, 128
Chou, R. C. Y., Peck, A. B., Lim, J., et al. 2007, ApJ, 670, 116
Condon, J. J., Helou, G., Sanders, D. B., & Soifer, B. T. 1996, ApJS, 103, 81
Cox, P., & Mezger, P. G. 1989, A&ARv, 1, 49
Dahlem, M., Golla, G., Whiteoak, J. B., et al. 1993, A&A, 270, 29
Dahlem, M., Weaver, K. A., & Heckman, T. M. 1998, ApJS, 118, 401
Draine, B. T., Dale, D. A., Bendo, G., et al. 2007, ApJ, 663, 866
Dumke, M., Nieten, C., Thuma, G., Wielebinsky, R., & Walsh, W. 2001, A&A, 373, 853
Eckhart, A., Cameron, M., Rothermel, H., Wild, W., & Zinnecker, H. 1990, ApJ, 363, 451
Engelbracht, C. W., Rieke, G. H., Gordon, K. D., et al. 2008, ApJ, 678, 804
Fabbiano, G. 1988, ApJ, 330, 672
Gardner, F. F., & Whiteoak, J. B. 1976, PASA, 3, 63
Güsten, R., Nyman, L., Schilke, P., et al. 2006, A&A, 454, 13
Hardcastle, M. J., Worrall, D. M., Kraft, R. P., et al. 2003, ApJ, 593, 169
Hardcastle, M. J., Kraft, R. P., & Worrall, D. M. 2006, MNRAS, 368, 15
Harrison, A., Henkel, C., & Russell, A. 1999, MNRAS, 303, 157
Houghton, S., Whiteoak, J. B., Koribalski, B., et al. 1997, A&A, 325, 923
Israel, F. P. 1998, A&ARv, 8, 237
Karachentsev, I. D., Tully, R. B., Dolphin, A., et al. 2007, AJ, 133, 504
Koribalski, B. S., Staveley-Smith, L., Kilborn, V. A., et al. 2004, AJ, 128, 16
Krügel, E., & Siebenmorgen, R. 1994, A&A, 288, 929
Krügel, E., Chini, R., Klein, U., et al. 1990, A&A, 240, 232
Kovacs, A. 2008, SPIE, 7020, in press
Leeuw, L. L., Hawarden, T. G., Matthews, H. E., Robson, E. I., & Eckart, A. 2002, ApJ, 565, 131
Madejski, G., Zycki, R., Done, C., et al. 2000, ApJ, 535, L87
Mauersberger, R., Henkel, C., Wielebinski, R., Wiklind, T., & Reuter, H.-P. 1996, A&A, 305, 421
McCaarthy, P. J., Heckman, T., & van Breugel, W. 1987, AJ, 92, 264
Melo, V. P., Perez Garcia, A. M., Acosta-Pulido, J. A., Munoz-Tunon, C., & Rodriguez Espinosa, J. M. 2002, ApJ, 574, 709
Mirabel, I. F., Laurent, O., Sanders, D. B., et al. 1999, A&A, 341, 667
Ott, M., Whiteoak, J. B., Henkel, C., & Wielebinski, R. 2001, A&A, 372, 463
Pilyugin, L. S., Contini, T., & Vilchez, J. M. 2004, A&A, 423, 427
Priddey, R. S., & McMahon, R. G. 2001, MNRAS, 324, 17
Radovich, M., Kahanpäa, J., & Lemke, D. 2001, A&A, 377, 73
Rekola, R., Richer, M. G., McCall, M. L., et al. 2005, MNRAS, 361, 330
Rieke, G. H., Harper, D. A., Low, F. J., & Armstrong, K. R. 1973, ApJ, 183, 67
Sakamoto, K., Ho, P. T. P., Iono, D., et al. 2006, ApJ, 636, 685
Siebenmorgen, R., & Krügel, E. 2007, A&A, 461, 445
Siringo, G., Weiß, A., Kreysa, E., et al. 2007, The Messenger, 129, 2
Sorai, K., Nakai, N., Kuno, N., Nishiyama, K., & Hasegawa, T. 2000, PASJ, 52, 785
Unger, S. J., Clegg, P. E., Stacey, G. J., et al. 2000, A&A, 355, 885
Wang, M., Henkel, C., Chin, Y. N., et al. 2004, A&A, 422, 883